Electrochimica Acta 251 (2017) 681–689

Contents lists available at ScienceDirect

Electrochimica Acta

journal homepage: www.elsevier.com/locate/electacta

Simulated impedance of diffusion in porous media

Samuel J. Cooper[a,*], Antonio Bertei[b], Donal P. Finegan[c,d], Nigel P. Brandon[b]

[a] Dyson School of Design Engineering, Imperial College London, London, SW7 1NA, UK
[b] Electrochemical Science and Engineering, Earth Science and Engineering, Imperial College London, London, SW7 2AZ, UK
[c] Electrochemical Innovation Lab, Department of Chemical Engineering, University College London, London WC1E 7JE, UK
[d] National Renewable Energy Laboratory, 15013 Denver West Parkway, Golden, CO 80401, USA

ARTICLE INFO

Article history:
Received 28 April 2017
Received in revised form 24 July 2017
Accepted 25 July 2017
Available online 27 July 2017

Keywords:
Impedance
Microstructure
Diffusion
Tomography
EIS
Warburg
TauFactor

ABSTRACT

This paper describes the use of a frequency domain, finite-difference scheme to simulate the impedance spectra of diffusion in porous microstructures. Both open and closed systems are investigated for a range of ideal geometries, as well as some randomly generated synthetic volumes and tomographically derived microstructural data. In many cases, the spectra deviate significantly from the conventional Warburg-type elements typically used to represent diffusion in equivalent circuit analysis. A key finding is that certain microstructures show multiple peaks in the complex plane, which may be misinterpreted as separate electrochemical processes in real impedance data. This is relevant to battery electrode design as the techniques for nano-scale fabrication become more widespread. This simulation tool is provided as an open-source MatLab application and is freely available online as part of the *TauFactor* platform.
© 2017 The Authors. Published by Elsevier Ltd. This is an open access article under the CC BY license (http://creativecommons.org/licenses/by/4.0/).

1. Introduction

Electrochemical impedance spectroscopy (EIS) is perhaps the most widely used technique for characterising electrochemical devices [1]. Either by fitting equivalent circuit models in the complex plane or by analysis of the distribution of relaxation times (DRT), it is possible to investigate and decouple the relative contributions to the impedance made by the various physical and electrochemical processes occurring in a cell [2].

Although cell electrodes are inherently three dimensional objects, the majority of elements in equivalent circuits (such as resistors, inductors and capacitors) are zero dimensional. Warburg elements are commonly used to model idealised one dimensional diffusion under a variety of boundary constraints. It is possible to find analytical solutions, or reasonable approximations, to many combinations of these boundary scenarios, such as Dirichlet (*i.e.*, specified concentration), Neumann (*i.e.*, specified flux) and semi-infinite [3]. This allows conventional fitting algorithms to incorporate Warburg elements, without the additional computational cost incurred by solving these domains numerically for each set of parameters.

However, the pseudo-1D nature of Warburg elements requires that the intricate details of real 3D microstructures must be summarised with only a few bulk parameters, such as the porosity and tortuosity factor. The tortuosity factor is a measure of the resistance to diffusive transport caused by convolutions in the flow paths [4]. As is shown later in this article, structures with very different morphologies can have identical tortuosity factors and porosities. However, analysing structures across a range of stimulation frequencies, as well as the usual steady-state analysis, enables some additional features of interest to be extracted that may be relevant to performance. Moreover, when analysing impedance data, it would be of interest to know whether the microstructure is responsible for deviations in the spectra away from the conventional Warburg model [5].

The effect of pore geometry on impedance was first modelled in detail in a 1976 paper by Keiser *et al.* [6], following on closely from the work of De Levie [7], where a pseudo-3D numerical model was used to generate impedance spectra for a range of closed pore geometries. The model uses a simplified transmission line assemblage of series resistors and branching capacitors, with the coefficients representing spatial distribution and axi-symmetry. The original paper is in German, but the concept was summarised for a wider audience in a review of EIS methods by Barsoukov and Macdonald [2], which also reframes it in the context of penetration depths. Raistrick [8] points out the limitations of the pseudo-3D approach and Eloot *et al.* [9] do

* Corresponding author.
E-mail address: samuel.cooper@imperial.ac.uk (S.J. Cooper).

http://dx.doi.org/10.1016/j.electacta.2017.07.152
0013-4686/© 2017 The Authors. Published by Elsevier Ltd. This is an open access article under the CC BY license (http://creativecommons.org/licenses/by/4.0/).

question the accuracy and relevance of Keiser's result; however, as these concerns are due in part to the assumptions required to make the calculation computationally feasible under the constraints of the day, it is reasonable to expect that the general trends would still be valid. Although over 40 years have passed since the Keiser paper, the authors of this work were unable to find an instance where the numerical results were directly used in the analysis of an EIS spectrum. This is likely due to both the unavailability of microstructural data and the computational expense of the simulation.

However, despite the uncertainty surrounding the link between EIS spectra and the geometry of microstructures, very many papers have cited Keiser, as well as its subsequent mentions in books and articles by Lasia [10–12], as a possible explanation for distortions in impedance spectra. Malko *et al.* [13] used EIS to investigate PEM carbon catalyst optimisation and attributed a deviation from the expected 45° slope to the pore broadening/narrowing phenomena discussed by Keiser. Noack *et al.* [14] also cited Keiser to explain variation in EIS results between samples of graphite felt electrodes. González-Buch *et al.* [15] used SEM image data to show that the templated pores in their metallic cathodes were narrowing cones, which lead them to conclude that their distorted EIS spectra could be explained by Keiser's findings. A study by Cericola and Spahr [16] analysed the effect of particle size, shape, and orientation on the performance of graphite electrodes and used Keiser's results to interpret a deviation from the expected 90° slope in the low frequency region of a blocked electrode. The degradation of silicon electrodes was investigated by Radvanyi *et al.* [17] and once again, they associate evolution of features in the EIS data to changes in the geometry of the system. A study by Wu *et al.* [18] on supercapacitor electrodes found an additional "arc-shaped" feature in their EIS data which they conclude, citing Keiser, to be the result of transport processes in "orbicular pores", after they systematically rule out other potential causes. Hitz and Lasia modelled "pear-shaped" pores similar to those investigated by Keiser and also observed a semi-cricle at high frequency, rather than the expected 45° slope [11]. As a final remark, Zhang *et al.* [19] highlighted the importance of the pore geometry for designing advanced supercapacitor electrodes, acknowledging that capturing non-uniform ion diffusion is crucial for high power performance. To clarify the cause of variation within the EIS spectra in each of the above cases, the material microstructures must be mapped in 3D and explored.

Recent advances in computed tomography (CT) have allowed the details of porous microstructures to be captured at high resolution [20–23]. This microstructural data is typically stored as cuboid voxels, each containing a grayscale value related to the local density or atomic mass of the sample, depending on the technique used. A segmentation approach must typically then be employed to convert this grayscale data into a labelled volume (although segmentation-free transport simulations are also possible [24]), representing the distribution of the various phases. As demonstrated in many recent studies [25–28], the segmented geometry data can then be used to calculate various microstructural parameters, such as the volume fractions, surface areas, triple phase boundary densities and tortuosity factors; all of which are of interest when trying to predict the performance of, for example, a porous electrochemical electrode

This article presents the implementation of a frequency domain finite-difference solver, suitable for segmented tomographic data, applied to calculate the diffusive impedance spectra of porous materials. First, an investigation of some idealised geometries is presented to aid the intuitive interpretation of the possible effects by analysing several simple open and closed systems. Following this, the method is applied to some real geometries, derived from tomographic data.

2. Method

2.1. Simulation

The solver used in this study is based on the finite-difference approach implemented in the open-source *TauFactor* platform recently released by the authors [24]. *TauFactor* was originally developed for quantifying diffusive tortuosity factors from segmented tomographic data by solving the steady-state diffusion equation between a pair of parallel Dirichlet boundaries. Although it is possible in principle to model a sinusoidal stimulation at one of the boundaries in the time domain, the computational cost would be prohibitive. In this study, the system was transformed into the frequency domain, where a sinusoidal stimulation is once again represented as a Dirichlet boundary condition. This approach allows the various optimization techniques already implemented in the *TauFactor* platform, such as over-relaxation, checkerboarding and vectorisation, to be used in the frequency domain, massively accelerating convergence (for more details, see [24]).

The system of equations in sys. (1) captures this steady-state diffusion problem in the frequency domain, including the fixed value (Dirichlet) conditions imposed at two parallel boundaries, where $Q = (0, L_x) \times (0, L_y) \times (0, L_z)$ is a cuboid in $\mathbb{R}^3$ and $\Omega \subset Q$ is the region of a porous medium inside Q where diffusion occurs. T, I and B are two-dimensional subsets of Q (*i.e.*, Top, Interfacial and Bottom), such that $\partial\Omega = T \cup I \cup B$ and $\partial\Omega|_{z=L_z} = B$, $\partial\Omega|_{z=0} = T$, $\partial\Omega|_{0<z<L_z} = I$. The complex distribution of the diffusing species through the porous medium Ω is then modelled by the solution to

$$\begin{cases} \nabla^2\hat{C} - \dfrac{i\omega}{D}\hat{C} = 0, & \text{in } \Omega, \\ \hat{C} = 0, & \text{on } T, \\ \nabla\hat{C}\cdot\mathbf{n} = 0, & \text{on } I, \\ \hat{C} = 1, & \text{on } B, \end{cases} \tag{1}$$

where $\mathbf{n}$ is the outward pointing unit normal to Ω; $\hat{C}$ is the complex concentration of the diffusing species; i is the imaginary unit; D is the intrinsic diffusivity of transporting phase (set to 1 in all cases); and ω is the frequency of the boundary stimulation, which is changed to calculate each point in a spectrum.

In the case where the top boundary is closed, the condition at boundary T simply becomes the same as boundary I. In all cases, convergence was measured by the stability of the complex impedance measured at the stimulated boundary, B.

In each simulation, a characteristic frequency, ω_c, was defined, around which the frequency range $[\omega_c \times 2^{-4}, \omega_c \times 2^{11}]$ was investigated.

$$\omega_c = \frac{D}{L^2} \tag{2}$$

where, for open systems, L is the length of the control volume (CV) in the direction normal to the stimulated surface and, for closed systems, L is equal to the maximum penetration distance from the stimulated surface to the tip of the longest pore path.

For each frequency, the impedance Z was calculated as the ratio between the amplitude of the concentration stimulus (1 in all cases) and the complex diffusion flux at the inlet boundary, and then normalised to $\tilde{Z}$ for ease of comparison by using Eq. (3).

$$\tilde{Z} = Z\frac{AD}{L} \tag{3}$$

where, for open systems, A is the total area of the CV boundary normal to the direction of flow and, for closed systems, A is the "mean accessible area", which is defined as the algebraic mean area accessible to diffusion at each discrete depth into the pore network. Using this formulation also means that the low frequency

intercept of open systems is equal to τ/ε, which is a useful characteristic feature for comparison between structures.

In order to initialise the simulation of open systems, the steady-state time-domain solution was found first and used as the low frequency intercept (*i.e.*, ω = 0). For closed systems, the low frequency initialisation involved setting all voxels in Ω to $\hat{C} = 1 + 0i$.

The physical interpretation of the transport equation and boundary conditions described above are those of idealised diffusion with either applied concentrations or zero fluxes at the boundaries. This simple system does not reflect the coupled multi-physics processes occurring in a real electrochemical electrode, such as contributions to transport from convection and electric migration, charge separation (*i.e.*, double layers) near the boundaries or concentrated solution effects, which would require more general transport models based on the Poisson-Nernst-Planck equations [29]. However, it is worth considering that these are the exact assumptions used in the standard Warburg model [30], which is widely used in EIS today. Furthermore, it is the simplicity of this system which allows for the system to be solved so quickly, using the tomography data directly as the nodes.

2.2. Example structures

The closed pore structures investigated in figure 4 of the article by Keiser *et al.* [6] were approximately recreated in 2D using MS Paint. These 2D templates were then used to produce voxelised axi-symmetric volumes through a simple rotation algorithm. Simulations were run on both the 2D (*i.e.*, prismatic) and 3D datasets. Due to the mirror symmetry of each structure in the direction normal to the stimulating boundary, only half the 2D structures (128 × 128 voxels) and quarter of the 3D volumes (128 × 128 × 128 voxels) were required for simulation. Straight (prismatic) closed pore systems are expected to recover the analytical Finite Space Warburg (FSW) solution and, similarly, prismatic open pore systems should recreate a Finite Length Warburg (FLW) solution.

Following this, a set of 6 new idealised 2D geometries were also created, through trial and error, each of which had the same volume fraction (ε = 0.5) as well as the same tortuosity factor (τ = 1.57) in the vertical direction of the white phase. At steady-state, these structures are indistinguishable in terms of their diffusive properties in the direction of interest; however, they would be expected to have distinct frequency spectra.

The "Sierpinski carpet" and "Pythagoras tree" 2D fractal structures were also investigated as they are commonly referenced in the literature as potential models for rough or multi-lengthscale systems [31–37]. An open boundary (FLW) was given to the Sierpinski carpets and, in order to converge to grid independent solutions, 5 × 5 voxel regions were used to represent the smallest squares, such that the sixth order carpet had the dimensions 3645 × 3645. The Pythagoras trees are closed systems (FSW) and only required 250 × 250 pixels to resolve their features. Due to the mirror symmetry of both fractals normal to the diffusion direction, only half the regions were required for simulation.

The fourth geometric category investigated was a 3D pseudo-random packing of spheres, which is a common model system for battery and fuel cell electrodes [38]. Although homogenisation approaches have been developed to represent these systems in 1D [39,40,30], extending this approach to 3D expands the design space for advanced electrodes by allowing for in-plane heterogeneity. The diffusion impedance from real battery systems typically comes from the solid phase diffusion in the radial direction within particles, rather than through the pore network [41,42]; however, anode-supported SOFCs can show losses from the extended, tortuous transport paths in the gas phase. The 3D packing of spheres was generated to have a linearly increasing porosity in the direction normal to the stimulated surface and it was analysed to develop a better understanding of what may be possible in reality.

Finally, two real tomographic datasets were also investigated, which were taken from a previous article by the authors on battery separator materials (Celgard 2325 and Celgard 2500) [43]. These structures where chosen because they have been manufactured to show a pronounced variation in porosity in the through-plane direction.

3. Results

Figure 1 shows the results of the simulated impedance calculations for the 2D and 3D creation of the 5 simple closed-pore geometries investigated by Keiser *et al.* [6].

The spectra of the seven 2D open-systems are shown in Fig. 2 . Each geometry has the same volume fraction of the white phase, as well as the same steady-state response in the time domain when an open boundary condition is used (*i.e.*, the same tortuosity

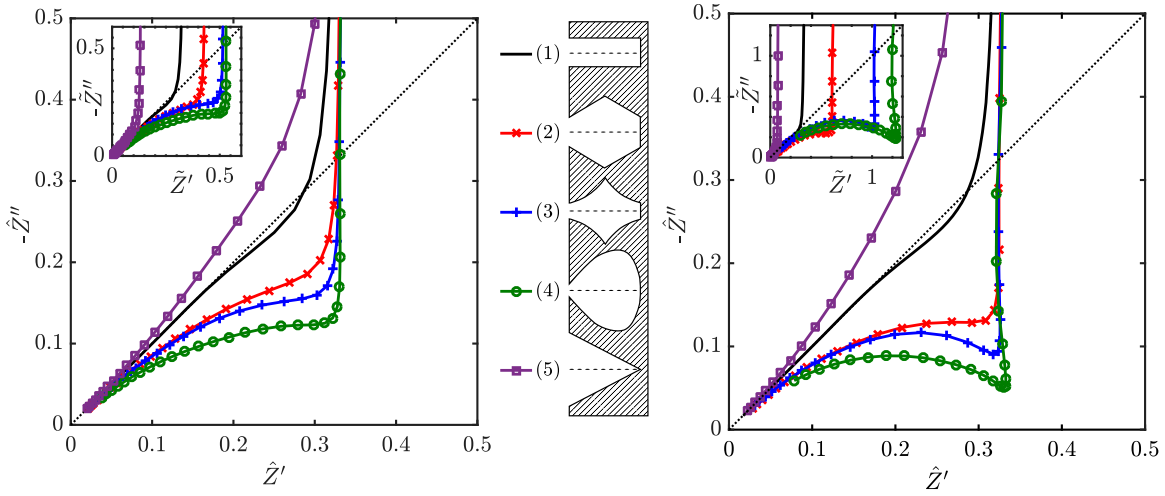

Fig. 1. Simulated impedance spectra for 2D (l) and 3D (r) recreations of the 5 simple closed-pore geometries investigated by Keiser *et al.* [6]. The inset graphs show the spectra as normalised using Eq. (3), whereas the main axes employ a second normalisation such that all spectra converge to the same value as the straight pore (1), to allow for clearer comparison of the shapes.

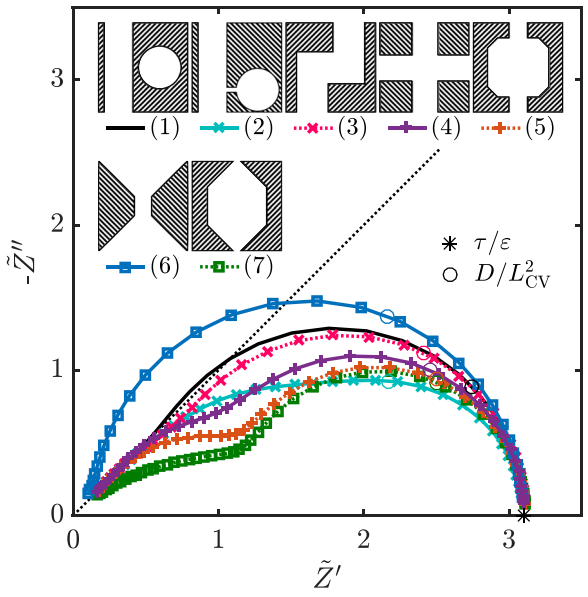

Fig. 2. Simulated impedance spectra of 7 simple open-pore geometries, each designed to have the same pore volume fraction and tortuosity factor in the direction normal to the stimulated boundary (vertical). The transport is occurring through the white phase of each geometry, with a constant zero concentration at the top surface and an applied sinusoidal concentration at the bottom.

factor). This means that based on current electrode equivalent circuit models, they would each be treated identically in terms of transport. However, simulated impedance reveals significant differences in their spectra.

Although geometry 1 in Fig. 2 has a straight diffusion path, its tortuosity factor is the same as the other geometries due to the region of isolated pore volume. However, the isolated volume simply has the effect of linearly scaling the spectra, so it will still be the same shape as the FLW solution, which is useful as a reference for interpreting the other shapes. The tortuosity factors of the other six geometries, although numerically identical, originate from a variety of combinations of constriction and path length convolution.

Figure 3 shows impedance plots for the first 6 orders of the two 2D fractal systems considered. The inset of the Sierpinski carpet graph shows the high frequency region in greater detail for the first and last geometries only.

The four impedance spectra resulting from the analysis of two tomographic datasets of battery separator materials are shown in Fig. 4 . The separators where imaged in a previous study by the authors [43], which showed them to have variable porosity in the through-plane direction. The axes of these two plots have been scaled such that the low frequency intercept of both samples aligns. Representative slices from the segmented tomographic images of the two samples are shown in the top right corner of each axis. Analytical spectra of FLW with the same low frequency intercepts are also plotted for comparison. Circles have been used to highlight the characteristic frequency of each spectrum.

Figure 5 shows the spectra obtained in a synthetic structure, generated by Monte Carlo algorithm [44], representing a 3D random packing of spherical particles linearly distributed along the vertical direction. The four simulations are obtained by flipping the packing, in order to have a linearly increasing or decreasing porosity along the diffusion direction, and considering either open or closed boundary condition at the top. The distribution of relaxation times for the two open structures, performed by using the DRTtools toolbox [45], is shown in the inset of Fig. 5.

4. Discussion

4.1. Comparison with pseudo-3D models

The results in the two plots in Fig. 1 show the same general trends as those described by Keiser *et al.*, despite the fact that the physics being modelled in the two studies is not identical. The Keiser *et al.* pseudo-3D model, as well as the models presented by de Levie [7] and Eloot *et al.* [9], consider the impedance generated by a pore filled with an electrolyte with finite ohmic resistivity surrounded by electrode walls having a specific surface capacitance. The diffusion impedance modelled in this study refers to a

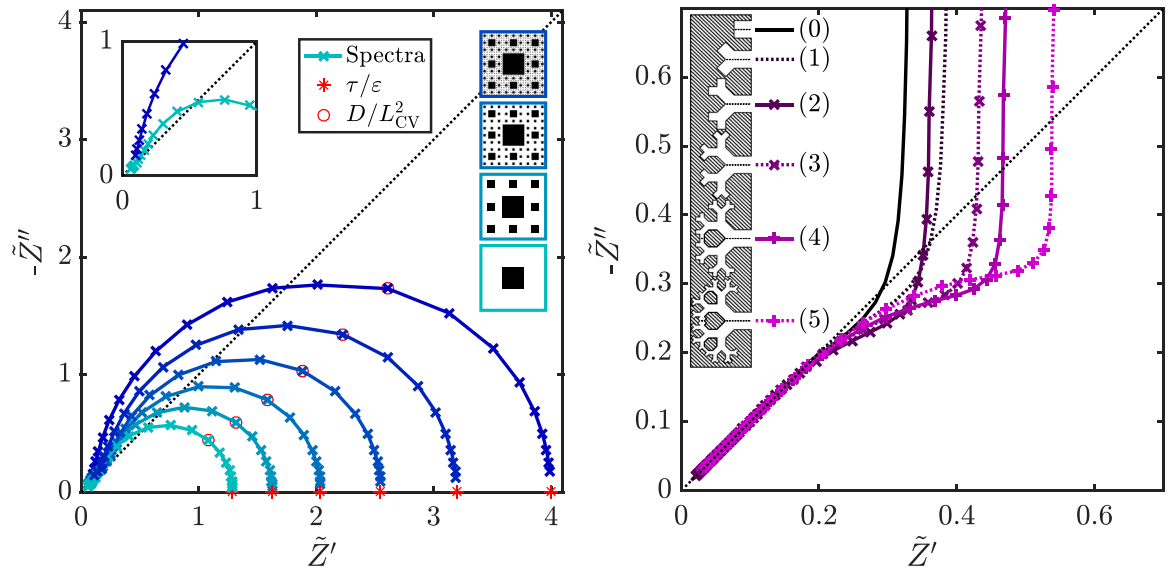

Fig. 3. Simulated impedance spectra of two 2D fractals, as the fractal order increases for (a) Sierpinski Carpet fractal with open boundaries and (b) Pythagoras Tree fractal with closed ends.

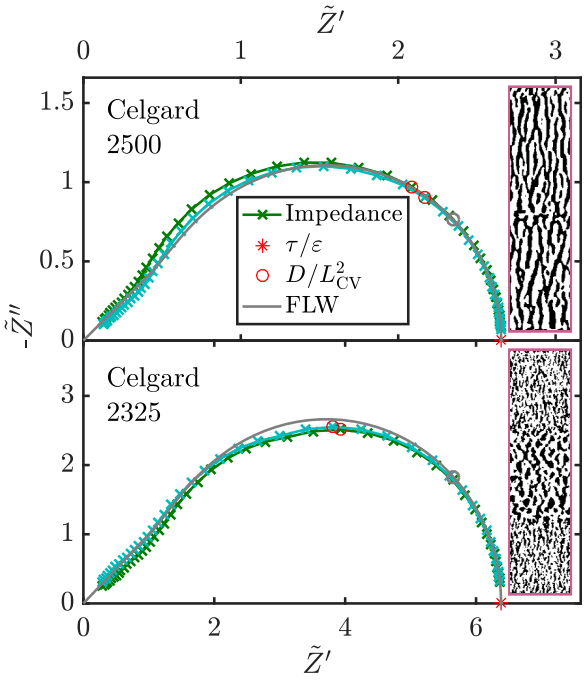

Fig. 4. Simulated impedance spectra through two tomographic datasets of battery separator materials from a paper by the authors [43]. The axes of these two plots have been scaled such that the low frequency intercept of both samples align. Each plot contains an inset showing a small region of the segmented tomographic data, where transport is in the vertical direction. Analytical spectra of FLW with the same low frequency intercepts are also plotted for comparison.

chemical species that diffuses within a pore having insulating walls. Despite these differences, the mathematical description of the two systems is remarkably similar, although the parameters governing the behaviour are clearly very different (see Appendix for more details). In particular, for straight cylindrical pores, these physical systems produce identical Warburg impedance spectra [3,46]. However, if the pore cross-section varies along the diffusion direction, minor differences in the two impedances occur. This is expected because in the case of the pseudo-3D model

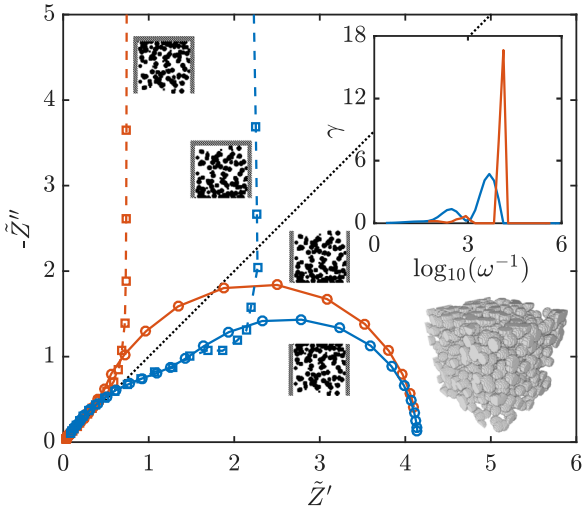

Fig. 5. Simulated impedance spectra for a synthetic packing of spherical particles with porosity linearly increasing (blue lines) or decreasing (red lines) from bottom to top. The top boundary can be either open (solid lines) or closed (dashed lines). The inset shows the DRT for the cases with open boundaries.

presented by Keiser *et al.*, the capacitance scales with the pore surface, while in the case presented here, the capacitance scales with the pore volume. Nevertheless, irrespective of the details of the transport model, Fig. 1 shows that the pore geometry has a measurable effect on the observed spectra, as further discussed in the next section.

Pseudo-3D models, such as those proposed by Keiser *et al.* or Eloot *et al.*, are expected to be less accurate than a full 2D/3D model, as presented in this study. In fact, pseudo-3D models neglect the curvature of equiconcentration planes in the direction normal to the macroscopic diffusion direction [8,47], thus assuming an infinite diffusion rate along such a normal direction. However, especially when the pore cross section broadens rapidly, equiconcentration planes are not perpendicular to the diffusion direction. Thus, while pseudo-3D models are limited by such a geometric simplification, which eventually leads to an underestimation of the impedance, the approach presented in this study improves the accuracy of impedance calculation without imposing a prohibitive computational cost. It is interesting to note that the results of Keiser *et al.* lie somewhere between the 2D and 3D cases simulated here, which is in keeping with the logic described above.

4.2. Effect of pore shape on diffusion impedance

The open systems investigated in Fig. 2 show a similarly marked deviation from the standard Warburg model, although, as these seven geometries were designed to have the same volume fraction and tortuosity factor, the spectra must all necessarily converge at both ends of the frequency range. As well as distorting the shape of the spectra, the geometry also had the effect of translating the characteristic frequency relative to that predicted by the analytical FLW solution.

The main difference in the shape of the spectra appears in the medium-high frequency range (centre-left of the complex plane). Geometries with a narrowing cross section along the diffusion direction (that is, moving away from the stimulated boundary), such as case 6, show an imaginary component of impedance larger than that expected from a conventional Warburg element. In other words, the phase is larger than 45°. On the other hand, geometries with a broadening diffusion path, such as case 7, show a phase always smaller than 45°. Such a behaviour at medium-high frequency, also reported by Keiser *et al.*, is present in the closed pore geometries analysed in Fig. 1, although there the impedance approaches a vertical asymptotic limit at low frequency due to the blocking boundary condition.

In order to explain such a behaviour, it is convenient to define the penetration depth [7,9,2], as follows:

$$l_\delta = \sqrt{\frac{D}{\omega}} \tag{4}$$

The penetration depth l_δ represents the characteristic length sampled by the alternating signal for a given frequency ω: as l_δ increases (that is, as the frequency decreases), the complex concentration $\hat{C}$ of the diffusing species penetrates deeper into the pore, sampling the volume further from the pore mouth (*i.e.*, the stimulated inlet boundary). When $l_\delta \approx L$ the concentration perturbation reaches the end of the pore, thus the boundary condition starts to affect the impedance: if the pore is open to an ideal reservoir (*i.e.*, boundary condition $\hat{C} = 0$), as in Fig. 2, then the impedance $\tilde{Z}$ approaches a finite real value and the phase becomes 0; if the pore end is blocking (*i.e.*, boundary condition $\nabla\hat{C}\cdot\mathbf{n} = 0$), as in Fig. 1, the imaginary component of the impedance $\tilde{Z}''$ goes to $\frac{-1}{\sqrt{2}\omega}$ and the phase approaches 90°, as shown by Song and Bazant [41].

These two opposite behaviours can be used to explain the impedance response at medium-high frequency in Fig. 2 for pores with a narrowing or broadening cross section. When the pore cross section narrows the diffusion flux is hindered, thus resembling the blocking wall boundary condition: as a consequence, the negative imaginary component of the diffusion impedance rises and the phase is larger than 45° (*e.g.*, Fig. 2, case 6). On the other hand, if the pore cross section broadens, the diffusion flux enters into a larger region, which resembles a reservoir, thus the imaginary component of diffusion impedance decreases and the phase becomes smaller than 45° (*e.g.*, Fig. 2, case 7). Therefore, the shape of the diffusion impedance in the complex plane can be related to the pore geometry, as similarly reported by Keiser *et al.* for a different physics.

The concept of penetration depth is also useful to explain the difference between the impedance response of cases 4, 5 and 7 in Fig. 2. All the pore shapes show a broadening cross section for the diffusing species, thus leading to a decrease in phase <45°. Since the broadening in case 7 is closer to the pore mouth than in cases 4 and 5, the departure from the 45° slope occurs for a smaller penetration depth l_δ in case 7, that is, for a larger frequency according to Eq. (4), as shown in Fig. 2. As the broadening is further from the pore mouth, as in cases 4 and 5, the frequency corresponding to the shift in phase becomes smaller.

Thus, since a change in pore cross section at a distance l_δ from the pore mouth is captured by a shift in phase in the complex plane, Eq. (4) can be used to estimate the expected frequency range where a distortion in diffusion impedance will be revealed given the diffusivity D and the feature size l_δ. For example, a sharp variation in pore geometry at a distance l_δ = 1, 10, 1000 μm from the pore inlet will be detected by diffusion impedance in the frequency range $\omega \approx 10^3$, 10, 10^{-3} Hz in a liquid ($D = 10^{-9}$ m s^{-2}) or $\omega \approx 10^7$, 10^5, 10 Hz in a gas ($D = 10^{-5}$ m s^{-2}), respectively.

The sequence of spectra in Fig. 3 a shows that as the order of the fractal increases, not only does its general resistance to transport increase (low frequency intercept) due to the more tortuous diffusion path, but there is also a change in shape of the high frequency region. In line with the results in Fig. 2, the approach towards the expected 45° line becomes increasingly steep as the severity of the path narrowing increases near the stimulated surface. Conversely, in Fig. 3 b as the fractal order increases, a larger area is available per unit penetration depth, increasing the extent to which the spectra stay below the 45° line in the medium-high frequency range, being in qualitative agreement with the depressed impedance arcs produced by hierarchical microstructures [31], systems with distributed pore sizes [48] or those with "secondary" pore networks [36,37].

4.3. Application to real 3D structures and some practical considerations

The spectra shown in Fig. 4, generated from tomographic volumes of battery separator materials, show that these kind of distortions can even be detected in real materials that are fairly homogeneous. Although the distortions observed are relatively modest compared to some of the synthetic geometries discussed earlier in the paper (in agreement with what has been previously reported by Candy *et al.* [49] for homogeneous spherical packings) they may still be noticeable in real EIS data. Beyond simply the distortion to the shape, the most pronounced difference between the spectra are the locations of the characteristic frequencies compared to the analytical FLW solution. One potential explanation for this is the relative contribution of extended path length and path constriction in the observed tortuosity factor. This would suggest that the Celgard 2325 structure has more convoluted flow paths, meaning that the frequency at which the full thickness of the system is probed is lower than the calculated value of ω_c. It is important to offer a cautionary note here that if the impedance spectrum of a tomographic dataset differs from the Warburg solution, but there is no reason to expect a variable porosity in the direction measured for the material as a whole, then the most likely explanation is that the volume analysed is too small and is not a representative sample. *TauFactor* already offers several methods to evaluate the minimum representative volume for a diffusion simulation.

More pronounced distortions are revealed in the synthetic packing structures with linearly distributed porosity as in Fig. 5. Functionally graded or multi-layered structures have been increasingly used for advanced electrodes in solid oxide fuel cells [50–53] and Li-ion batteries [54,55], although this approach has received some criticism [56]. For such highly heterogeneous structures, the impedance response of diffusing species differs remarkably from the conventional Warburg behaviour, as in Fig. 5. For example, the open structure with linearly increasing porosity (solid blue line) appears to have two distinct peaks, reflective of two different time constants. It is worth restating here, to avoid any confusion, that this model does not consider any electrochemistry and that the two observed peaks are both from a purely diffusive process. Figure 5 also contains an inset showing the distribution of relaxation times (DRT) for the two open systems. Although the DRT spectrum for a FLW is expected to have many peaks, the secondary peak is especially pronounced in this structure. Since DRT analysis is increasingly used as a screening tool to identify the number of physical/electrochemical processes to be associated with equivalent circuit elements [57], such a pronounced peak due merely to the diffusion in an anisotropic microstructure might be misinterpreted for an additional electrochemical process, thus leading to a misuse of extra equivalent circuit elements as already discussed by Bertei *et al.* [58].

Hence, once the electrode microstructure is known, for example through computed tomography as in Fig. 4, the impedance response due to the diffusion phenomena can be evaluated and subtracted from the experimental spectra to focus on the other electrochemical phenomena of interest. Notably, the approach can be reversed: provided that diffusion be the main phenomenon taking place in the electrode, diffusion impedance can be used as a tool to infer microstructural information, similar to what is currently done with electrochemical porosimetry [59,60]. This is certainly possible to some extent, as shown in the previous section regarding the shift in phase for narrowing or broadening cross sections, yet with some limitations. In fact, any heterogeneity in the porous structure does produce a feature in the complex plane at a frequency roughly equal to the corresponding penetration depth (Eq. (4)), but different signals become more convoluted as l_δ increases and are eventually affected by the pore-end boundary condition for $l_\delta \approx L$: beyond this penetration depth, that is, for frequencies $\omega < \omega_c$, the quality of microstructural information that can be inferred from diffusion impedance worsens dramatically. This means that heterogeneous features in the pore structure are better resolved when closer to the pore inlet at high frequency (*i.e.*, for $\omega > \omega_c$). Moreover, the same diffusion impedance fingerprint can be produced by different families of microstructures, thus the reconstruction of the porous structure from diffusion impedance is not unequivocally determined. On the other hand, relevant microstructural metrics regarding the pore geometry can be distinguished, such as the narrowing/broadening of cross section or decrease/increase in porosity as shown in Figs. 2 and 5.

This paper is intended to showcase the simulated impedance technique, but future studies will aim to analyse representative volumes of tomographic data and compare these to measured EIS spectra.

5. Conclusions

The simulation approach presented in this paper allows the effect of geometry on diffusion to be calculated and compared to the conventional Warburg elements commonly used in equivalent circuit models. The results for simple closed pore geometries agree well with those presented by Keiser *et al.* . This study extends the work of Keiser *et al.* to include open systems, for which similar deviations from the spectra of the simple 1D case were also observed. The simulation tool has been integrated into the *TauFactor* platform, which is specifically designed for the analysis of tomographic data.

Analysis of battery separator material tomography datasets showed minor deviations from the standard Warburg solution, depending on the direction analysed, while larger deviations are revealed in synthetic electrodes with graded porosity or with fractal geometry. The tool presented in this study is thus essential for the understanding, deconvolution and prediction of the diffusion impedance response in heterogeneous porous media, especially for advanced electrodes with engineered microstructure.

Acknowledgements

This project has received funding from the European Union's Horizon 2020 research and innovation programme under the Marie-Skłodowska-Curie grant agreement No 654915 and the EPSRC grants EP/M014045/1 and EP/K002252/1. The authors would like to thank Gavin Reade, Dr Vladimir Yufit, Prof. Anthony Kucernak and Prof. Alan Atkinson for useful discussions on EIS and microstructure, as well as Dr Paul Shearing for the use of tomography data acquired in his laboratory. Disclaimer: the European Commission Research Executive Agency is not responsible for any use that may be made of the information this paper contains.

Appendix A.

The three-dimensional diffusion problem can be reduced to a pseudo-3D model in order to show the similarities with the models presented by Keiser *et al.* and Eloot *et al.* .

Let us call x the main direction of diffusion flux in the porous domain. Assuming that the pore is axisymmetric and equiconcentration planes are normal to the diffusion direction x, the governing equation can be reduced to an ordinary differential equation as follows:

$$\begin{cases} i\omega\hat{C}\pi r^2 \mathrm{d}x = -\dfrac{\mathrm{d}}{\mathrm{d}x}\left(-D\dfrac{\mathrm{d}\hat{C}}{\mathrm{d}x}\pi r^2\right)\mathrm{d}x, & \text{in } 0 < x < L, \\ \hat{C} = 1, & \text{at } x = 0, \\ \begin{cases} (\mathrm{FLW}): & \hat{C} = 0, \\ (\mathrm{FSW}): & -D\dfrac{\mathrm{d}\hat{C}}{\mathrm{d}x} = 0, \end{cases} & \text{at } x = L, \end{cases} \tag{A.1}$$

where r represents the local pore radius, which is a function of x.

System (A.1) can be recast in dimensionless form after defining the dimensionless coordinate $\tilde{x} = x/L$, the dimensionless radius $\tilde{r} = r/r_0$ (where r_0 is the pore radius at $x = 0$), and the characteristic frequency $\omega_c = \frac{D}{L^2}$ as follows:

$$\begin{cases} \dfrac{\mathrm{d}^2\hat{C}}{\mathrm{d}\tilde{x}^2} + \dfrac{2}{\tilde{r}}\dfrac{\mathrm{d}\tilde{r}}{\mathrm{d}\tilde{x}}\dfrac{\mathrm{d}\hat{C}}{\mathrm{d}\tilde{x}} - i\dfrac{\omega}{\omega_c}\hat{C} = 0, & \text{in } 0 < \tilde{x} < 1, \\ \hat{C} = 1, & \text{at } \tilde{x} = 0, \\ \begin{cases} (\mathrm{FLW}): & \hat{C} = 0, \\ (\mathrm{FSW}): & \dfrac{\mathrm{d}\hat{C}}{\mathrm{d}\tilde{x}} = 0, \end{cases} & \text{at } \tilde{x} = 1. \end{cases} \tag{A.2}$$

Let us now consider the impedance of an axisymmetric pore filled with an electrolyte, having constant conductivity σ, surrounded by electrode walls with specific surface capacitance c, which is the same physics studied by Keiser *et al.* and Eloot *et al.*.

The pseudo-3D model of such a system is as follows:

$$\begin{cases} i\omega c\hat{V}2\pi r\mathrm{d}x = -\dfrac{\mathrm{d}}{\mathrm{d}x}\left(-\sigma\dfrac{\mathrm{d}\hat{V}}{\mathrm{d}x}\pi r^2\right)\mathrm{d}x, & \text{in } 0 < x < L, \\ \hat{V} = 1, & \text{at } x = 0, \\ \begin{cases} (\mathrm{FLW}): & \hat{V} = 0, \\ (\mathrm{FSW}): & -\sigma\dfrac{\mathrm{d}\hat{V}}{\mathrm{d}x} = 0, \end{cases} & \text{at } x = L, \end{cases} \tag{A.3}$$

where $\hat{V}$ is the complex electric potential.

By considering the same dimensionless groups already defined in Eq. (A.2), with the only exception for the characteristic frequency $\omega_c = \frac{\sigma r_0}{2cL^2}$, Eq. (A.3) becomes:

$$\begin{cases} \dfrac{\mathrm{d}^2\hat{V}}{\mathrm{d}\tilde{x}^2} + \dfrac{2}{\tilde{r}}\dfrac{\mathrm{d}\tilde{r}}{\mathrm{d}\tilde{x}}\dfrac{\mathrm{d}\hat{V}}{\mathrm{d}\tilde{x}} - i\dfrac{\omega}{\omega_c}\dfrac{\hat{V}}{\tilde{r}} = 0, & \text{in } 0 < \tilde{x} < 1, \\ \hat{V} = 1, & \text{at } \tilde{x} = 0, \\ \begin{cases} (\mathrm{FLW}): & \hat{V} = 0, \\ (\mathrm{FSW}): & \dfrac{\mathrm{d}\hat{V}}{\mathrm{d}\tilde{x}} = 0, \end{cases} & \text{at } \tilde{x} = 1. \end{cases} \tag{A.4}$$

Equation (A.4) is very similar to the reduced diffusion model reported in Eq. (A.2), where $\hat{V} = \hat{C}$; $\sigma = D$ and $\frac{2c}{r_0} = 1$. The only difference is in the $\frac{1}{\tilde{r}}$ factor in the rightmost term of Eq. (A.4). Such a factor comes from the fact that in this system the capacitance scales with the pore surface while in the diffusion problem the mass-capacitance scales with the pore volume. However, when the pore radius is constant ($\tilde{r} = 1$), eqs. (A.2) and (A.4) are identical, thus they produce the same Warburg impedance response irrespective of the different physics, except for a few dimensional scaling factors, which do not affect the impedance shape in the complex plane.

The accuracy of the pseudo-3D model becomes questionable as the assumption of equiconcentration planes perpendicular to diffusion direction no longer holds, such as for ratios of top to bottom cross section (A_T/A_B) much different from 1 as reported in Fig. 6 . In such a case, the pseudo-3D model i) underestimates the diffusion resistance $Z'(\omega = 0)$ and ii) overestimates the frequency dependence (*i.e.*, $\varphi(\omega)$) shifts slightly on the right towards larger

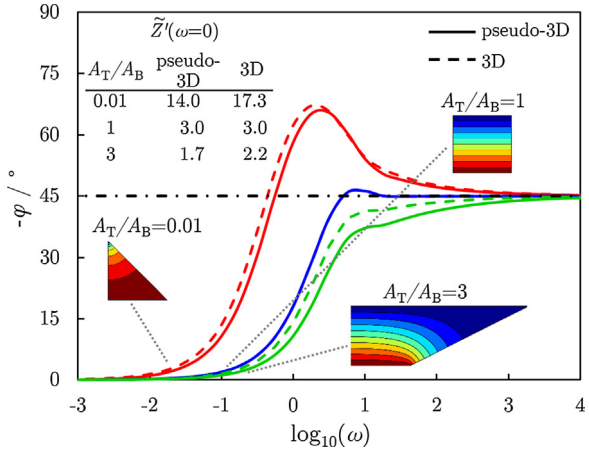

Fig. 6. Simulated phase angle against log frequency for three simple microstructures each with a different ratio of the inlet to outlet area.

frequencies) in comparison with the 3D model. This is due to the fact that, in 3D and in reality, the diffusion flux perpendicular to x is finite (that is, not infinite as assumed in pseudo-3D), thus resulting in a larger resistance and larger timescale than what predicted by the pseudo-3D model.

References

[1] D.D. MacDonald, Reflections on the history of electrochemical impedance spectroscopy, Electrochimica Acta 51 (2006) 1376–1388.
[2] E. Barsoukov, J.R. Macdonald, Impedance Spectroscopy: Theory, Experiment, and Applications, 2nd Edition, (2005) .
[3] U. Tröltzsch, O. Kanoun, Generalization of transmission line models for deriving the impedance of diffusion and porous media, Electrochimica Acta 75 (2012) 347–356.
[4] N. Epstein, On tortuosity and the tortuosity factor in flow and diffusion through porous media, Chemical Engineering Science 44 (1989) 777–779.
[5] J. Landesfeind, J. Hattendorff, A. Ehrl, W.A. Wall, H.A. Gasteiger, Tortuosity Determination of Battery Electrodes and Separators by Impedance Spectroscopy, Journal of The Electrochemical Society 163 (2016) A1373–A1387.
[6] H. Keiser, K.D. Beccu, M.A. Gutjahr, Abschätzung der porenstruktur poröser elektroden aus impedanzmessungen, Electrochimica Acta 21 (1976) 539–543.
[7] R. de Levie, On porous electrodes in electrolyte solutions: I. Capacitance effects, Electrochimica Acta 8 (1963) 751–780.
[8] I. Raistrick, Impedance studies of porous electrodes, Electrochimica Acta 35 (1990) 1579–1586.
[9] K. Eloot, F. Debuyck, M. Moors, A.P. Van Peteghem, Calculation of the impedance of noncylindrical pores Part I: Introduction of a matrix calculation method, Journal of Applied Electrochemistry 25 (1995) 326–333.
[10] A. Lasia, Electrochemical Impedance Spectroscopy and its Applications, volume 1, (2014) .
[11] C. Hitz, A. Lasia, Experimental study and modeling of impedance of the her on porous Ni electrodes, Journal of Electroanalytical Chemistry 500 (2001) 213–222.
[12] R. Jurczakowski, C. Hitz, A. Lasia, Impedance of porous Au based electrodes, Journal of Electroanalytical Chemistry 572 (2004) 355–366.
[13] D. Malko, T. Lopes, E.A. Ticianelli, A. Kucernak, A catalyst layer optimisation approach using electrochemical impedance spectroscopy for PEM fuel cells operated with pyrolysed transition metal-N-C catalysts, Journal of Power Sources 323 (2016) 189–200.
[14] J. Noack, G. Cognard, M. Oral, M. Küttinger, N. Roznyatovskaya, K. Pinkwart, J. Tübke, Study of the long-term operation of a vanadium/oxygen fuel cell, Journal of Power Sources 326 (2016) 137–145.
[15] C. González-Buch, I. Herraiz-Cardona, E. Ortega, J. García-Antón, V. Pérez-Herranz, Study of the catalytic activity of 3D macroporous Ni and NiMo cathodes for hydrogen production by alkaline water electrolysis, Journal of Applied Electrochemistry 46 (2016) 791–803.
[16] D. Cericola, M.E. Spahr, Impedance Spectroscopic Studies of the Porous Structure of Electrodes containing Graphite Materials with Different Particle Size and Shape, Electrochimica Acta 191 (2016) 558–566.
[17] E. Radvanyi, W. Porcher, E. De Vito, A. Montani, S. Franger, S. Jouanneau Si Larbi, Failure mechanisms of nano-silicon anodes upon cycling: an electrode porosity evolution model, Physical Chemistry Chemical Physics 16 (2014) 17142.
[18] H. Wu, X. Wang, L. Jiang, C. Wu, Q. Zhao, X. Liu, B. Hu, L. Yi, The effects of electrolyte on the supercapacitive performance of activated calcium carbide-derived carbon, Journal of Power Sources 226 (2013) 202–209.
[19] Y. Zhang, L. Liu, On Diffusion in Heterogeneous Media, American Journal of Science 312 (2013) 1028–1047.
[20] D.S. Eastwood, R.S. Bradley, F. Tariq, S.J. Cooper, O.O. Taiwo, J. Gelb, A. Merkle, D. J.L. Brett, N.P. Brandon, P.J. Withers, P.D. Lee, P.R. Shearing, The application of phase contrast X-ray techniques for imaging Li-ion battery electrodes, Nuclear Instruments and Methods in Physics Research Section B: Beam Interactions with Materials and Atoms 324 (2014) 118–123.
[21] N. Ni, S.J. Cooper, R. Williams, N. Kemen, D.W. McComb, S.J. Skinner, Degradation of (La 0.6 Sr 0.4) 0.95 (Co 0.2 Fe 0.8)O 3-δ Solid Oxide Fuel Cell Cathodes at the Nanometer Scale and below, ACS Applied Materials & Interfaces 8 (2016) 17360–17370.
[22] L. Holzer, B. Iwanschitz, T. Hocker, B. M??nch, M. Prestat, D. Wiedenmann, U. Vogt, P. Holtappels, J. Sfeir, A. Mai, T. Graule, Microstructure degradation of cermet anodes for solid oxide fuel cells: Quantification of nickel grain growth in dry and in humid atmospheres, Journal of Power Sources 196 (2011) 1279–1294.
[23] P. Pietsch, V. Wood, X-Ray Tomography for Lithium Ion Battery Research: A Practical Guide, Annu. Rev. Mater. Res 47 (2017) 12.1-12.29.
[24] S.J. Cooper, A. Bertei, P.R. Shearing, J.A. Kilner, N.P. Brandon, TauFactor: An open-source application for calculating tortuosity factors from tomographic data, SoftwareX 5 (2016) 203–210.
[25] P.R. Shearing, N.P. Brandon, J. Gelb, R. Bradley, P.J. Withers, A.J. Marquis, S.J. Cooper, S.J. Harris, Multi Length Scale Microstructural Investigations of a Commercially Available Li-Ion Battery Electrode, Journal of the Electrochemical Society 159 (2012) A1023–A1027.
[26] J. Joos, M. Ender, I. Rotscholl, N.H. Menzler, E. Ivers-Tiffée, Quantification of double-layer Ni/YSZ fuel cell anodes from focused ion beam tomography data, Journal of Power Sources 246 (2014) 819–830.
[27] F. Tariq, M. Kishimoto, S.J. Cooper, P.R. Shearing, N.P. Brandon, Advanced 3D Imaging and Analysis of SOFC Electrodes, ECS Transactions 57 (2013) 2553–2562.
[28] Y.C. Karen Chen-Wiegart, J.S. Cronin, Q. Yuan, K.J. Yakal-Kremski, S.a. Barnett, J. Wang, 3D Non-destructive morphological analysis of a solid oxide fuel cell anode using full-field X-ray nano-tomography, Journal of Power Sources 218 (2012) 348–351.
[29] J.R. Macdonald, Utility and Importance of Poisson-Nernst-Planck Immittance-Spectroscopy Fitting Models, The Journal of Physical Chemistry C 117 (2013) 23433–23450.
[30] S. Devan, V.R. Subramanian, R.E. White, Analytical Solution for the Impedance of a Porous Electrode, Journal of The Electrochemical Society 151 (2004) A905.
[31] M. Eikerling, A.A. Kornyshev, E. Lust, Optimized Structure of Nanoporous Carbon-Based Double-Layer Capacitors, Journal of The Electrochemical Society 152 (2005) E24.
[32] J. Schröttle, A. Dörnbrack, Turbulence structure in a diabatically heated forest canopy composed of fractal Pythagoras trees, Theoretical and Computational Fluid Dynamics 27 (2013) 337–359.
[33] A. Ebrahimi Khabbazi, J. Hinebaugh, A. Bazylak, Analytical tortuosity-porosity correlations for Sierpinski carpet fractal geometries, Chaos, Solitons & Fractals 78 (2015) 124–133.
[34] T.C. Halsey, M. Leibig, The double layer impedance at a rough electrode: a random walk method, Electrochimica Acta 36 (1991) 1699–1702.
[35] M. Leibig, T.C. Halsey, The double-layer impedance at a rough surface: numerical results, Journal of Electroanalytical Chemistry 358 (1993) 77–109.
[36] Y. Gourbeyre, B. Tribollet, C. Dagbert, L. Hyspecka, A Physical Model for Anticorrosion Behavior of Duplex Coatings, Journal of The Electrochemical Society 153 (2006) B162.
[37] M. Itagaki, Y. Hatada, I. Shitanda, K. Watanabe, Complex impedance spectra of porous electrode with fractal structure, Electrochimica Acta 55 (2010) 6255–6262.
[38] G.M. Goldin, A.M. Colclasure, A.H. Wiedemann, R.J. Kee, Three-dimensional particle-resolved models of Li-ion batteries to assist the evaluation of empirical parameters in one-dimensional models, Electrochimica Acta 64 (2012) 118–129.
[39] M. Doyle, J.P. Meyers, J. Newman, Computer Simulations of the Impedance Response of Lithium Rechargeable Batteries, Journal of The Electrochemical Society 147 (2000) 99.
[40] J.P. Meyers, M. Doyle, R.M. Darling, J. Newman, The Impedance Response of a Porous Electrode Composed of Intercalation Particles, Journal of The Electrochemical Society 147 (2000) 2930.
[41] J. Song, M.Z. Bazant, Effects of Nanoparticle Geometry and Size Distribution on Diffusion Impedance of Battery Electrodes, Journal of the Electrochemical Society 160 (2013) A15–A24.
[42] J. Song, M.Z. Bazant, Electrochemical Impedance of a Battery Electrode with Anisotropic Active Particles, Electrochimica Acta 131 (2014) 214–227.
[43] D.P. Finegan, S.J. Cooper, B. Tjaden, O.O. Taiwo, J. Gelb, G. Hinds, D.J.L. Brett, P.R. Shearing, Characterising the structural properties of polymer separators for lithium-ion batteries in 3D using phase contrast X-ray microscopy, Journal of Power Sources 333 (2016) 184–192.
[44] C. Chueh, A. Bertei, J. Pharoah, C. Nicolella, Effective conductivity in random porous media with convex and non-convex porosity, International Journal of Heat and Mass Transfer 71 (2014) 183–188.
[45] T.H. Wan, M. Saccoccio, C. Chen, F. Ciucci, Influence of the Discretization Methods on the Distribution of Relaxation Times Deconvolution: Implementing Radial Basis Functions with DRTtools, Electrochimica Acta 184 (2015) 483–499.
[46] M. Bazant, Electrochemical Energy Systems, Spring 2011, in: Electrochemical Energy Systems, volume 626, MIT OpenCourseWare, 2011.
[47] J. Gunning, The exact impedance of the de Levie grooved electrode, Journal of Electroanalytical Chemistry 392 (1995) 1–11.
[48] M. Musiani, M. Orazem, B. Tribollet, V. Vivier, Impedance of blocking electrodes having parallel cylindrical pores with distributed radii, Electrochimica Acta 56 (2011) 8014–8022.
[49] J.-P. Candy, P. Fouilloux, M. Keddam, H. Takenouti, The characterization of porous electrodes by impedance measurements, Electrochimica Acta 26 (1981) 1029–1034.
[50] D. Simwonis, H. Thülen, F. Dias, A. Naoumidis, D. Stöver, Properties of Ni/YSZ porous cermets for SOFC anode substrates prepared by tape casting and coat-mix® process, Journal of Materials Processing Technology 92 (1999) 107–111.
[51] Y. Liu, C. Compson, M. Liu, Nanostructured and functionally graded cathodes for intermediate temperature solid oxide fuel cells, Journal of Power Sources 138 (2004) 194–198.
[52] E.S. Greene, W.K. Chiu, M.G. Medeiros, Mass transfer in graded microstructure solid oxide fuel cell electrodes, Journal of Power Sources 161 (2006) 225–231.
[53] S.W. Sofie, Fabrication of Functionally Graded and Aligned Porosity in Thin Ceramic Substrates With the Novel Freeze?Tape-Casting Process, Journal of the American Ceramic Society 90 (2007) 2024–2031.
[54] V. Ramadesigan, R.N. Methekar, F. Latinwo, R.D. Braatz, V.R. Subramanian, Optimal Porosity Distribution for Minimized Ohmic Drop across a Porous Electrode, Journal of The Electrochemical Society 157 (2010) A1328.
[55] S. Golmon, K. Maute, M.L. Dunn, A design optimization methodology for Li+ batteries, Journal of Power Sources 253 (2014) 239–250.

[56] Y. Dai, V. Srinivasan, On Graded Electrode Porosity as a Design Tool for Improving the Energy Density of Batteries, Journal of The Electrochemical Society 163 (2016) A406–A416.
[57] A. Weber, S. Dierickx, A. Kromp, E. Ivers-Tiffée, Sulfur Poisoning of Anode-Supported SOFCs under Reformate Operation, Fuel Cells 13 (2013) 487–493.
[58] A. Bertei, G. Arcolini, C. Nicolella, P. Piccardo, Effect of Non-Uniform Electrode Microstructure in Gas Diffusion Impedance, ECS Transactions 68 (2015) 2897–2905.
[59] H.-K. Song, Y.-H. Jung, K.-H. Lee, L.H. Dao, Electrochemical impedance spectroscopy of porous electrodes: the effect of pore size distribution, Electrochimica Acta 44 (1999) 3513–3519.
[60] H.-K. Song, J.-H. Sung, Y.-H. Jung, K.-H. Lee, L.H. Dao, M.-H. Kim, H.-N. Kim, Electrochemical Porosimetry, Journal of The Electrochemical Society 151 (2004) E102.